

Article

## High Resolution Mapping of Peatland Hydroperiod at a High-Latitude Swedish Mire

Nathan Torbick <sup>1,\*</sup>, Andreas Persson <sup>2</sup>, David Olefeldt <sup>3</sup>, Steve Frolking <sup>4</sup>, William Salas <sup>1</sup>, Stephen Hagen <sup>1</sup>, Patrick Crill <sup>5</sup> and Changsheng Li <sup>4</sup>

<sup>1</sup> Applied Geosolutions, 403 Kent Place, Newmarket, NH 03824, USA;

E-Mails: wsalas@appliedgeosolutions.com (W.S.); shagen@appliedgeosolutions.com (S.H.)

<sup>2</sup> Department of Physical Geography and Ecosystem Sciences, Lund University, Sölvegatan 12, SE-22100 Lund, Sweden; E-Mail: andreas.persson@nateko.lu.se

<sup>3</sup> Department of Integrative Biology, University of Guelph, Science Complex, Guelph, ON N1G 2W1, Canada; E-Mail: dolefeld@uoguelph.ca

<sup>4</sup> Earth Systems Research Center, Institute for the Study of Earth, Oceans, and Space, University of New Hampshire, 8 College Road, Durham, NH 03824, USA;

E-Mails: steve.frolking@unh.edu (S.F.); changsheng.li@unh.edu (C.L.)

<sup>5</sup> Department of Geological Sciences, Stockholm University, 10691 Stockholm, Sweden; E-Mail: patrick.crill@geo.su.se

\* Author to whom correspondence should be addressed; E-Mail: torbick@appliedgeosolutions.com.

Received: 28 April 2012; in revised form: 7 June 2012 / Accepted: 26 June 2012 /

Published: 29 June 2012

---

**Abstract:** Monitoring high latitude wetlands is required to understand feedbacks between terrestrial carbon pools and climate change. Hydrological variability is a key factor driving biogeochemical processes in these ecosystems and effective assessment tools are critical for accurate characterization of surface hydrology, soil moisture, and water table fluctuations. Operational satellite platforms provide opportunities to systematically monitor hydrological variability in high latitude wetlands. The objective of this research application was to integrate high temporal frequency Synthetic Aperture Radar (SAR) and high spatial resolution Light Detection and Ranging (LiDAR) observations to assess hydroperiod at a mire in northern Sweden. Geostatistical and polarimetric (PLR) techniques were applied to determine spatial structure of the wetland and imagery at respective scales (0.5 m to 25 m). Variogram, spatial regression, and decomposition approaches characterized the sensitivity of the two platforms (SAR and LiDAR) to wetland hydrogeomorphology, scattering mechanisms, and data interrelationships. A Classification and Regression Tree (CART),

based on random forest, fused multi-mode (fine-beam single, dual, quad pol) Phased Array L-band Synthetic Aperture Radar (PALSAR) and LiDAR-derived elevation to effectively map hydroperiod attributes at the Swedish mire across an aggregated warm season (May–September, 2006–2010). Image derived estimates of water and peat moisture were sensitive ( $R^2 = 0.86$ ) to field measurements of water table depth (cm). Peat areas that are underlain by permafrost were observed as areas with fluctuating soil moisture and water table changes.

**Keywords:** PALSAR; LiDAR; mire; hydroperiod; high latitude wetlands; permafrost

---

## 1. Introduction

Trends in climate change and permafrost degradation in northern high latitudes have raised questions over the potential greenhouse gas emissions response from permafrost, lakes, and wetlands. Northern high latitude soils contain approximately 1,000 petagrams (Pg) of carbon in the top 3 m [1]. Changing climate is likely to increase vulnerability of this soil carbon [2], and could alter net CO<sub>2</sub> and CH<sub>4</sub> emissions significantly [3–5]. One of the primary drivers of net emissions in peatlands response is hydrological flux and water balance, which can influence both rates of methane and carbon dioxide emissions and of permafrost thaw [6,7]. Therefore, accurate spatiotemporal information on hydrological variability is critical for assessing peatland emissions response to climate change.

Remote sensing can provide a powerful tool for assessing landscape hydrology at large spatial scales and in remote regions. Efforts to improve understanding of hydrological variability and high latitude wetlands have utilized Synthetic Aperture Radar (SAR). The advantages of SAR relative to optical sensors include the ability to penetrate vegetation canopies, a direct sensitivity to water and vegetation structure, and the capacity for observation in all weather conditions. The Phased Array L-band Synthetic Aperture Radar (PALSAR) instrument onboard the Advanced Land Observing Satellite (ALOS-1) was one such platform with a mission to provide regional and consistent (regular overpass collections) microwave data collection. The relatively long L-band wavelength (23.5 cm, 1.275 GHz), as compared to C- or X-band, enables the capture of different scattering mechanisms that make detecting flood status in different wetland types (*i.e.*, herbaceous, forested, emergent, grassland) feasible with high accuracies [8–13]. Recent efforts have also highlighted L-band advantages over C-band when using techniques that apply phase differencing and decomposition of scattering to effectively discriminate detailed wetland classes and monitor peat thickness and wetness [14,15].

While ALOS-1 is no longer collecting data, the archives of ALOS-1 PALSAR provide five years of observations at multiple scales and modes. This includes fine-beam single and dual (FBS/D) pol (HH, HH+HV) observations along with a polarimetric (PLR) mode (HH+HV+VH+VV) at ground resolutions on the order of 6.25 m to 24 m, respectively, with adequate signal-to-noise ratios for mapping hydroperiod. In this application, hydroperiod is defined as the frequency and duration of inundation or flooding. The planned launch of ALOS-2, scheduled to continue L-band collections in 2013, will have even more advanced capabilities. Concordantly, other high resolution platforms will likely become operational that can provide complementing observations, such as Light Detection and

Ranging (LiDAR) data. LiDAR uses a laser pulse sent from above that interacts with surface features and returns. From this process information can be extracted including precise elevation or land surface topography along with canopy structure metrics. The ability to collect LiDAR at a fine-scale has led to many wetland and wetland hydrology applications, such as the mapping of topographic attributes and flow paths (e.g., [16,17]), and planned operational LiDAR platforms are underway. The fusion of these different remotely sensed data for characterizing aquatic ecosystems will continue to expand as research applications seek to extract and combine the individual strengths (*i.e.*, spatial resolution, spectral coverage, temporal frequency) of SAR, LiDAR, optical, and ancillary spatial datasets such as soil or climate information (e.g., [18–21]).

The use of high temporal frequency (e.g., daily–weekly), finer-scale (e.g., <25m) SAR for mapping high latitude peatland hydroperiod has potential to improve our understanding of dynamics and climate change response. Further, operational techniques that fuse multiple high-resolution platforms (e.g., PALSAR, LiDAR) need to be developed for integrating the strengths of multiple sensors for wetlands assessment and monitoring. The overarching goal of this research application was to assess hydroperiod at a high latitude wetland using fine-scale, multi-mode PALSAR and LiDAR observations. Spatial structure of the data and the high latitude wetland were characterized using a geostatistical approach. A Classification and Regression Tree was developed to take advantage of all available SAR and LiDAR, independent of mode or scale, to generate fused hydroperiod maps. The geospatial products were integrated with field data to provide a comprehensive assessment of the site. The approach was designed to be easily scalable, transferable, and to potentially be implemented in an operational context to support assessment and monitoring of wetland response to climate change as similar platforms (e.g., SMAP, ALOS-2, ICESat-2) come online.

## 2. Methods

### 2.1. Study Area

Stordalen mire (68°21'20"N, 19°2'47"E) is located adjacent to Lake Tornetrask, about 10 km east of Abisko, and approximately 250 km north of the Arctic Circle, in northern Sweden. Mean annual air temperature is  $-0.7$  °C and mean annual precipitation is 304 mm, based on long-term weather data collected at the Abisko Scientific Research Station. Land cover was categorized into general classes such as (1) hummock/mosses and ground scrub-shrub or palsa (dry ombrotrophic), (2) mesic (ombro-minerotrophic), (3) open water, and (4) graminoid (wet minerotrophic). Other classes such as occasional patches of barren soil and rock exposure were not included as a specific class. The majority of the mire has fen-like conditions, with a portion underlain by a subsurface permafrost zone [22]. Permafrost can be defined as ground that is below 0 °C for consecutive years while the active layer (surface thaw) is not permafrost although below the active layer is permafrost, or subsurface permafrost. Palsas underlain by permafrost and vegetated with low stature shrubs, are elevated about 1m above the wet-vegetated surfaces. As permafrost thaws, the palsas collapse into mesic or wet vegetation conditions.

## 2.2. Geofield Photos

Field-level photos were collected using a GPS-enabled camera (“geofield photos”). A stratified random sampling scheme focused on dominant covers was carried out in the mire during Day Of Year (DOY) 242-245 in 2010. A practical line-intercept approach was executed where an individual transects the site considering location of paths, instrumentation, and sensitivity of the site. Nadir and directional photos were taken during the walking transect across the site. All geofield photos were linked to shape files and keyhole markup language (KML) files to store, display, and share photos. KML files use a tag based structure with attributes that allow display. These photos are available for viewing and sharing in Google Earth or any GIS platform at <http://www.eomf.ou.edu/photos>. At this website users can search and share a library of global georeferenced field photos for product development and validation [23]. The purpose of the geofield photos for this application was to help guide image interpretation and analysis.

## 2.3. Instrumentation

Precipitation, temperature, and water table depth (WTD) were collected at the mire from instrumentation and field work [24,25]. Daily weather and flux data from tower instrumentation at the site were collected between 2002 and 2010 including maximum and minimum air temperature ( $^{\circ}\text{C}$ ) and precipitation (mm). Water table depth (cm) was measured between DOY 130 to 251 between 2003 and 2010. Two tubes were embedded into the mire at a wet site and mesic site to delineate water table levels. Temporal data gaps exist due to logistical constraints and costs of frequent site visits. Data were aggregated to compare to concordant PALSAR overpass periods. The data collected from instrumentation was used to help characterize hydroperiod and image interpretation (Figure 1).

**Figure 1.** Tower instrumentation data illustrating: (a) daily maximum and minimum air temperature ( $^{\circ}\text{C}$ ) with precipitation (mm) on 2nd axis (right) across Day Of Year (DOY) for 2008, (b). water table depth at representative mesic (M) and wet (W) mire locations for 2008 and 2009, respectively, across DOY, (c). soil moisture (SM) percent for representative palsa (P) and sphagnum bog (S) sites with evapotranspiration (mm/day) on 2nd axis (right) across DOY for 2008, and (d). net ecosystem exchange (NEE) and gross ecosystem productivity (GEP) ( $\mu\text{mol}\cdot\text{C}\cdot\text{m}^{-2}\cdot\text{s}^{-1}$ ) with average daily temperature ( $^{\circ}\text{C}$ ) on primary axis across DOY for 2008.

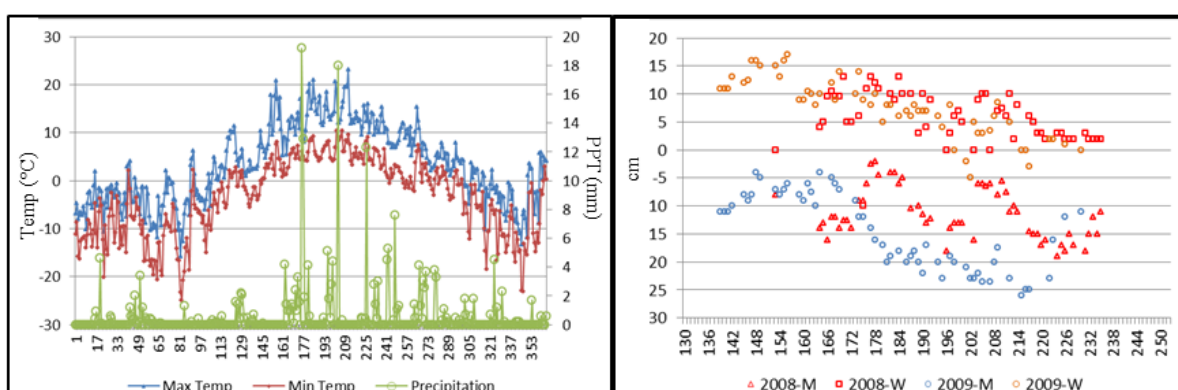
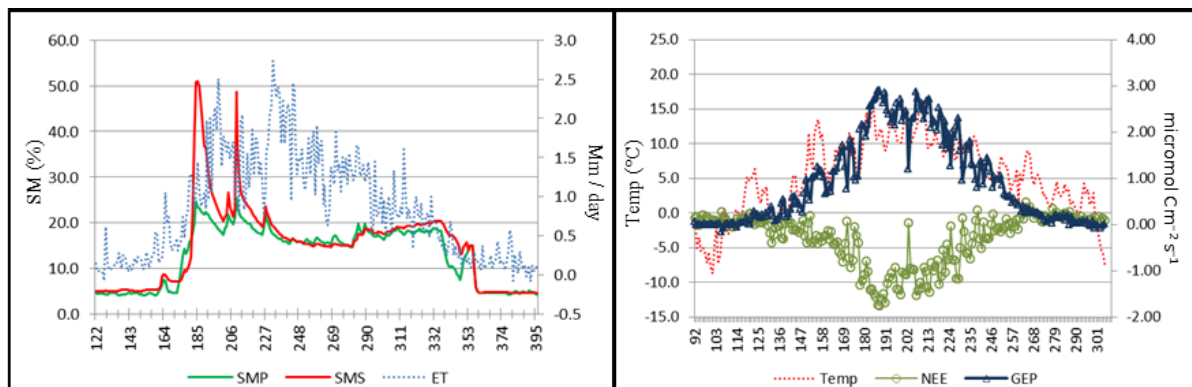


Figure 1. Cont.



#### 2.4. LiDAR and DEM

LiDAR and Digital Elevation Model (DEM) data were used to process SAR observations and assist in characterizing mire hydrogeomorphic attributes. Some very high latitude regions, such as the Stordalen mire, have limited coverage by traditional DEMs. Shuttle Radar Topography Mission (SRTM) data does not exist at this latitude. Therefore, large-area elevation data at 50 m spacing for the Stordalen site was obtained from Lantmäteriet (Swedish mapping and cadastral authority, product number: 5802) to assist in terrain geocoding since the finebeam PALSAR stamps cover approximately 75 km × 75 km. Very high spatial resolution (13 points·m<sup>-2</sup>) elevation data for the site was obtained from an airborne LiDAR collection over a small portion of the key area of the mire. The LiDAR collection was carried out on DOY 214 of 2008. Spatial autocorrelation tests showed that inverse distance weighted (IDW) interpolations were adequate for generating a hierarchical suite (0.5 m, 1 m, 5 m) of DEM products (elevation, slope, flow accumulation) for the site from the LiDAR data [17]. The highest resolution LiDAR products were used in this application.

#### 2.5. Fine-Beam PALSAR Preprocessing

L-band SAR data was obtained through the Kyoto and Carbon Initiative of the Japan Aerospace Exploration Agency (JAXA) ALOS-1 platform (Table 1). PALSAR images were ordered via the ALOS User Interface Gateway (AUIG: <https://auig.eoc.jaxa.jp>) operated by JAXA. Onboard ALOS is the PALSAR instrument operating in fine-beam mode with single (HH) and dual polarizations (HH+HV) along with full polarimetry (HH+HV+VH+VV). The center frequency is 1270 MHz (23.6 cm), with a 28 MHz bandwidth in fine beam single polarization mode, and 14 MHz in the dual, quad-pol, and ScanSAR modes. The off-nadir angle is variable between 21 ° and 50.8 ° (at mid-swath).

High temporal frequency (~weekly intervals by using multiple years) fine-beam single- (FBS) and dual- (FBD) pol observations were collected in Single Look Complex (SLC) at 34.3 and 41.5 incident angles. The collection period focused on the warm seasons during 2006 to 2010. Images were collected in SLC to optimize the complete signal and adjust the effective number of looks considering the ground range resolution, the pixel spacing in azimuth, and incidence angle. Images were co-registered using a cubic convolution cross-correlation approach considering shifts in range and azimuth dependency. A multitemporal de Grandi filter, that strives to preserve temporal signatures while

reducing speckle by applying an optimum weighting filter that balances differences in signals between different times [26,27], was applied to remove spatially random multiplicative noise (speckle). Multitemporal filtering was conducted with observations from the same geometry before terrain geocoding. All PALSAR imagery utilized covered the entire mire area.

**Table 1.** Remotely sensed data used for analyses with observation date, mode (fine-beam single (S), fine beam dual (D), quad/polarimetric (Q), and off nadir angle ( $\theta$ ), shown for the Swedish mire site.

<u>Platform</u>	<u>Date</u>	<u>DOY</u>	<u>Mode</u>	<u><math>\theta</math></u>
PALSAR	5/31/2007	151	Q	21.5
PALSAR	6/10/2006	161	S	41.5
PALSAR	6/27/2006	178	S	41.5
PALSAR	7/2/2007	183	D	34.3
PALSAR	7/19/2007	200	D	34.3
PALSAR	7/27/2010	208	D	34.3
PALSAR	8/12/2006	224	D	41.5
PALSAR	8/17/2007	229	D	34.3
PALSAR	8/22/2009	234	D	34.3
PALSAR	8/29/2006	241	D	41.5
PALSAR	9/3/2007	246	D	34.3
PALSAR	9/11/2010	254	D	34.3
PALSAR	9/27/2006	270	S	41.5
LiDAR	8/7/2009	219	-	
Sweden DEM	-	-	-	

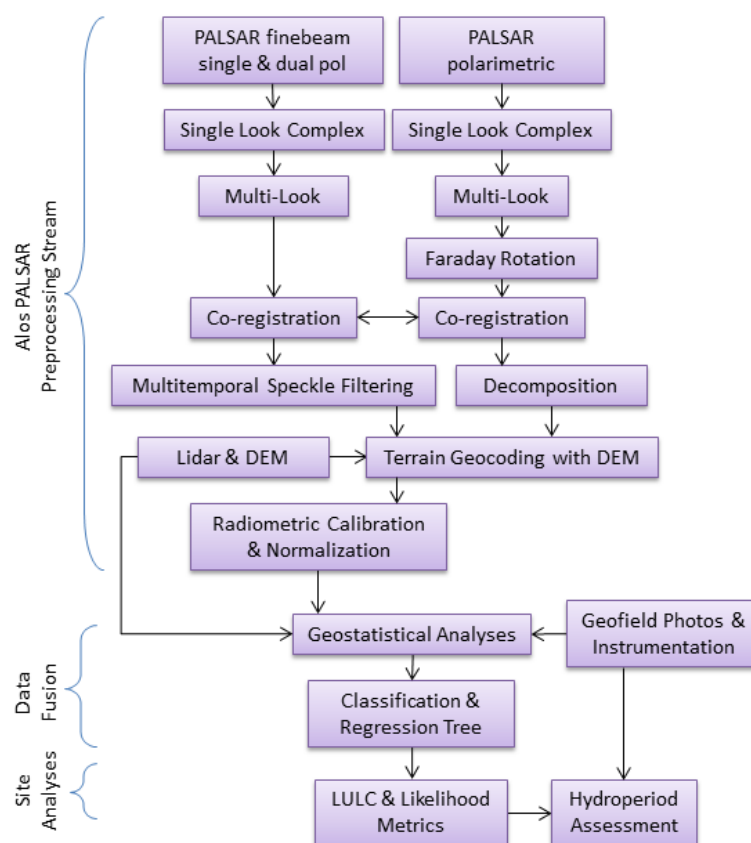
Terrain geocoding used the best available large-area digital elevation model (DEM) for the study site and followed the range-Doppler approach. Images were radiometrically calibrated and normalized by eliminating local incident angle effects and antenna gain and spread loss patterns to provide 6.25 m, 12.5 m, and 25 m (ground spatial resolution) sigma nought ( $\sigma^{\circ}$ ) image products. Local incidence angle and layover/shadow maps were generated for potential post classification processing to adjust for poor data pixels; however, in general the mire area is relatively flat at the scale of the ground resolution of the preprocessed PALSAR. The purpose of multitemporal PALSAR imagery was to map water extent, phenology, and mire hydroperiod.

## 2.6. Polarimetric PALSAR Preprocessing

The PLR imagery was obtained in similar fashion as the FBS/D imagery for DOY 151 (05/31/2007) at 21.5 off nadir angle. The primary advantage of utilizing PLR observations is the increase in the number of “bands” which permits a more thorough characterization of the scattering mechanisms by supplying more information compared to single or dual pol observations alone. Many research and application studies have carried out target scattering decomposition with PLR observations to map biogeophysical features [28,29]. In this application three well-established decomposition routines were executed to characterize properties of the mire with each routine chosen for a strategic purpose. The Pauli decomposition was applied to help visualize the primary scattering mechanism at the site. This is a common technique used to characterize coherent scatterers based on the scattering matrix [28,30].

The Cloude-Pottier (CP) decomposition was applied to generate entropy, anisotropy, and alpha parameters based on the coherence matrix [30]. These CP parameters provide a metric of the scattering mechanisms of the mire, the significance of non-dominant scatterers, and the primary scatterer at the mire. The final PLR technique applied was the Touzi decomposition which has recently been shown to effectively map high latitude wetland composition and peatland soil moisture [29,31]. Faraday rotation was applied to multilooked data before generating the decomposition products to correct for atmospheric conditions or depolarization caused by the faraday effect [32]. Products were then used to characterize the scattering mechanisms of the mire and hydrological attributes.

**Figure 2.** Flow diagram of multitemporal PALSAR integrated with LiDAR and field data to assess mire hydroperiod and surface conditions.



## 2.7. Analytical Approach

The analysis was carried out in two primary stages to characterize mire hydrogeomorphology. The first stage carried out geostatistical assessment to characterize data interrelationships and spatial structure across the mire. The second stage carried out a classification routine to map hydroperiod at the mire (Figure 2). The initial step in the first analysis stage applied variogram methods to the fully preprocessed PALSAR and LiDAR products to understand spatial structure of the data and mire. The use of variograms to help guide image processing and landscape analysis has been shown to be useful in other high resolution wetland assessments [33]. Variogram models were used to identify spatial dependency and landscape structure of the mire as measured by the remote sensing platforms (*i.e.*, PALSAR and LiDAR). This approach helps evaluate whether spatial structure needs to be considered

when pre-processing imagery. Second, the variograms were used to describe potential spatial structure or trends of the mire, as observed from the remotely sensed observations at respective scales (0.5 m, 6.25 m, 12.5 m, 25 m), to characterize surface hydrology and scales of processes. Third, the variogram technique was used in conjunction with interpretation and topographic wetness indices generated from LiDAR [17] to provide an additional method to quantify mire patterns in a spatially-aware approach.

### 2.7.1. Geostatistical Analyses

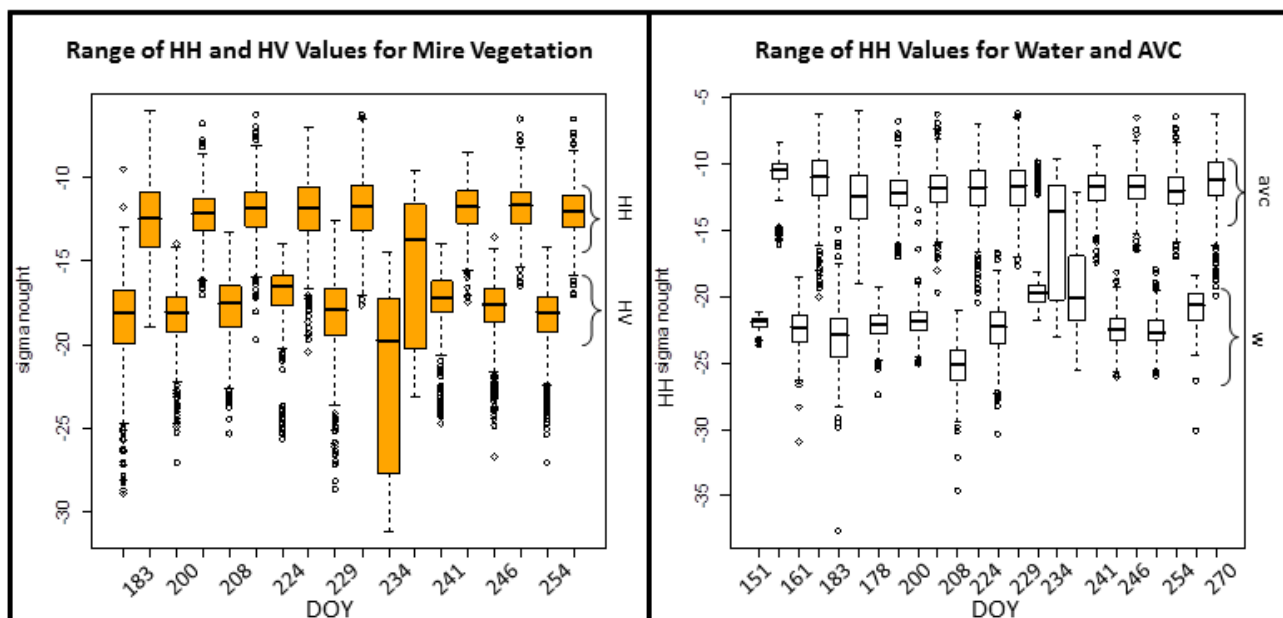
Spatial regression was then carried out between LiDAR elevation, PALSAR backscatter (dB), and decomposition products to compliment the variogram assessment. Noted here is the use of “decomposition” techniques applied in remote sensing methodologies to extract biogeophysical attributes of interest as opposed to decomposition processes of soil organic matter and plant litter in wetland ecosystems. The LiDAR was considered the independent variable with PALSAR as dependent to understand the degree to which elevation was influencing the recording of scatter mechanisms, or in a sense influencing mire community composition and configuration due to surface topography. Three different regression models were evaluated in an effort to best approximate the relationship between the remote sensing observations. The three models considered were ordinary least squares (OLS), a spatial lag model, also known as a spatial autoregressive ( $S_pAR$ ) model, and a spatial error model (SEM). The OLS model assumes spatial independence of the dependent variables and the error terms or residuals of the model. The  $S_pAR$  model accounts for the presence of spatial autocorrelation in the dependent variable, but assumes spatial independence of the error terms. The SEM allows for spatial dependence of the error terms. More detailed descriptions can be found in Anselin [34] and Anselin and Bera [35]. OLS estimates tend to be overstated in the presence of spatial autocorrelation, so the spatially-explicit  $S_pAR$  and SEM models were considered as alternatives because of their ability to incorporate spatial autocorrelation. The optimum spatial regression approach was determined by using a set of lagrange multiplier diagnostic criteria as recommended by Anselin [34].

### 2.7.2. Classification and Regression Tree

The second stage of the analysis used a Classification and Regression Tree (CART) to ingest all available high-resolution data for characterizing the landscape. CART techniques have substantial advantages for remote sensing problems because of their flexibility, intuitive simplicity, and computational efficiency. The CART model was constructed to take advantage of the various data sources and resolutions (e.g., 0.5 m, 6.25 m, 12.5 m, 25 m) to generate maps of hydroperiod at the respective scales. Each DOY has the PALSAR overpass for that DOY along with Lidar generated DEM and slope products as input into the CART model. For example, on DOY 151 inputs into the CART included decomposition information (Touzi, CP, Pauli), LiDAR generated products (elevation, slope), and quad pol PALSAR sigma nought backscatter (HH, HV, VH, VV) imagery; while, inputs on DOY 161 included single pol PALSAR sigma nought backscatter (HH) and LiDAR products (elevation, slope). Table 1 lists all the data that was used as input for the CART; LiDAR was paired with the PALSAR overpass for its given DOY overpass. The CART algorithm was implemented in the R statistical software package in the context of a “randomForest”. A random forest is generated through the creation of a series of CARTs using bagging, or resampling with replacement. Random forest algorithms

have been shown to be powerful classifiers in a range of applications [36]. Lawrence *et al.* [37] and Watts *et al.* [38] have recently had success in applying this nonparametric, bagging technique for classifying landscapes in Montana and Alaska, respectively. Recently, Whitcomb *et al.* [39] describe the use of a randomForest CART technique to successfully generate a high-resolution, synoptic map of wetlands across Alaska using L-band observation from the Japanese Earth Resources Satellite 1 (JERS-1).

**Figure 3.** Box and whisker plots illustrating fine-beam dual pol ( $HH\sigma^\circ$  and  $HV\sigma^\circ$ ) vs DOY for aggregated vegetation classes (**left**) and water (w) vs. aggregated vegetation classes (avc) for  $HH\sigma^\circ$  highlighting distinction between the classes (**right**).



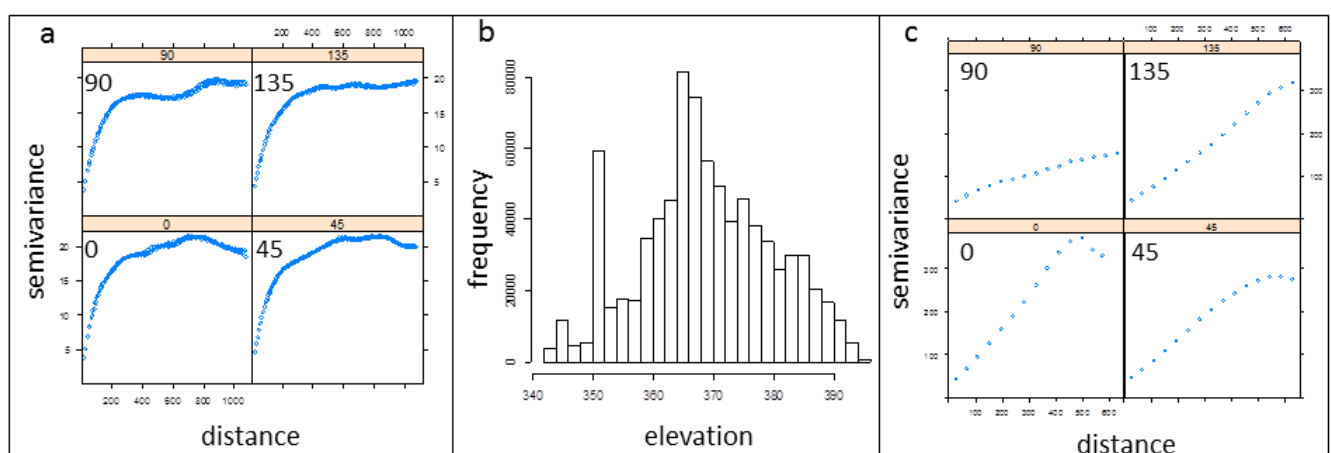
Training data for the CART, in the form of polygons, were created within a GIS by using the geofield photos to interpret patches of dominant covers types (identified in the study site description) in the imagery. Box and whisker plots were used to visualize the distribution of HH and HV values as a function of DOY for each wetlands class and for aggregate wetlands classes (Figure 3). Training data within each polygon were randomized into subsets to create many “trees” with the number of trees dependent on the ratio of observations (*i.e.*, pixels in polygons) between classes (*i.e.*, water vs. hummock/palsa). In other words, training polygons remained spatially consistent across the DOY inputs while the total number of training pixels used to represent a class may differ due to pixel size and/or training area. Therefore, a procedure to randomize the sampling and construct training classes was carried out. These trees were not pruned at this stage. Each tree was made up of a series of nodes based on the various input parameters for each observation period (*i.e.*, DOY 151 inputs); therefore, each DOY was its own “tree” within the “forest” with the data available for a given DOY as input into the CART. The rules are designed to split the data into sub-groups maximizing differentiation. The splitting stops when no further gain in differentiation can be made. In the end, every new pixel for prediction was run through the “forest” made up of trees and each tree casts a vote. A series of iterations in this fuzzy classification procedure generate a likelihood metric based on the number of votes for a particular class. Here, the term ‘likelihood’ is used to refer to the frequency a pixel is

determined (voted) to best match each class (e.g., water or hummock/palsa or graminoid or mesic). Final CART output included error matrix accuracy statistics using out-of-sample data (*i.e.*, data not used to train the CART), a thematic map with the dominant class for each tree (e.g., DOY), and class maps with the numbers of times each class (*i.e.*, water) received a vote. As a final analysis step the CART products were compared against WTD measurements to assess hydroperiod at the mire over time and space.

### 3. Results and Discussion

The variograms indicate landscape structure and measure the spatial autocorrelation in the remotely sensed imagery at the given resolutions of the PALSAR (6.25–25 m) and Lidar (1 m) (Figure 4). The fine-beam single and dual pol terrain geocoded PALSAR imagery found no major structural features at the scale of the mire as evident in the variograms which are primarily isotropic across the different DOY intervals and different fine-beam modes (HH or HV) with no drastic points of inflection. When modeling the larger region several large waterbodies created non-stationarity and first order drift. Therefore, the results and discussion are focused on the mire itself and exclude all regional drivers. Minor inflection along the sill was present when moving from high elevations toward lower elevations. Strong spatial dependence (correlation) was observed at the mire at a range of several hundred meters with relatively steep slope and modest nugget discontinuity considering the fine scale of the SAR data. Gradual ecotonal shifts were present in structure, as observed from the multitemporal filtered, fine-beam data indicating the ability to distinguish “pure pixels” and vegetative structure of major wetland classes and larger patches, considering the range which the sill begins to level off. In other words, there are pixels with mixed surface vegetation at the scale of the PALSAR observations.

**Figure 4.** Directional variogram for PALSAR HH on DOY 224 (a) shows, in general, major structural features, as measured by fine-beam dual pol PALSAR backscatter, are primarily isotropic. Strong spatial dependence is observed at the mire at a range of several hundred meters. Relatively normal distribution of LiDAR (b) at mire highlights several relatively large water pools at elevation ~350 m a.s.l. Directional variogram of LiDAR DEM (c) shows strong anisotropic behavior in the 135 direction indicating surface pathways.



A summary of spatial regression results are presented in Tables 2–4. The OLS results between LiDAR-derived elevation (independent variable), PALSAR sigma nought (dB) backscatter (dependents), and PLR decomposition products (dependents) indicate significant albeit weak correlation (Table 2). OLS regression is based on an underlying assumption that the error terms are independent and identically distributed with a mean of zero and constant variance. The strength of the LiDAR to “predict” PALSAR was weak as indicated by the  $R^2$ ; implying elevation or topography are not strong determinates of scattering mechanisms as observed from the PALSAR. Diagnostic testing of the OLS results show that these underlying assumptions are violated, however. The lagrange multiplier (LM) diagnostics (Table 3) indicate that there is spatial autocorrelation in the error terms (LMerr). The highly significant paired LM diagnostics (*i.e.*, LMerr and LMLag) and the corresponding robust (RLM) diagnostics were all significant; since the robust LMerr (RLMerr) statistics were greater than the corresponding RLMLag statistics, it was concluded that the spatial error model (SEM) was most appropriate to evaluate the relationship between LiDAR-derived elevation and each of the dependent variables. Results of the SEM are summarized in Table 4. The spatial autocorrelation coefficient (Lambda) was very strong across PALSAR products and likelihood ratio (LR) testing was found significant. This confirms the presence of spatial autocorrelation observed in the directional variograms. Furthermore, the Akaike Information Criterion (AIC) value for the SEM was lower than the AIC value for the OLS model in all cases; this indicates that the SEM provides a better fit to the data than the OLS model. These patterns were typical across modes and DOY. These results imply that at the given scales of the data and ecological processes the LiDAR-derived elevation is not a strong predictor of backscatter or PLR derived scattering mechanisms; however, modest significant ability to predict is present. Ecologically, this implies that elevation changes influence vegetative patterns at the mire, although the remotely sensed data found the relationship weak due to the scales of the SAR data.

**Table 2.** Representative Ordinary Least Squares regression analysis with FBD DOY 224 and PLR 151 highlighted.

Dependent Variable	Independent Variable	Regression Coefficient	Standard Error	t Statistic	p-value	R-squared	AIC
HH	(Intercept)	−27.251	1.644	−16.58	<2e-16	0.02	25,321.58
	B1	0.039	0.004	8.75	<2e-16	--	--
HV	(Intercept)	−51.407	1.347	−38.15	<2e-16	0.11	23,355.99
	B1	0.093	0.004	25.22	<2e-16	--	--
Entropy	(Intercept)	0.427	0.043	10.02	<2e-16	0.00	−10,805.38
	B1	0.000	0.000	−2.61	0.01	--	--
Anisotropy	(Intercept)	0.187	0.042	4.45	0.00	0.00	−10,930.04
	B1	0.000	0.000	2.66	0.01	--	--
Alpha	(Intercept)	2.373	0.105	22.52	<2e-16	0.05	−1,846.56
	B1	−0.005	0.000	−16.00	<2e-16	--	--

**Table 3.** Diagnostic testing for representative spatial autocorrelation.

Dependent Variable	Diagnostic Test	Test Statistic	Degrees of Freedom	p-value
HH	LMerr	49226.20	1	<2.2E-16
	LMlag	48392.94	1	<2.2E-16
	RLMerr	1043.69	1	<2.2E-16
	RLMlag	210.43	1	<2.2E-16
HV	LMerr	86181.20	1	<2.2E-16
	LMlag	67040.78	1	<2.2E-16
	RLMerr	19444.34	1	<2.2E-16
	RLMlag	303.92	1	<2.2E-16
Entropy	LMerr	34566.95	1	<2.2E-16
	LMlag	34368.03	1	<2.2E-16
	RLMerr	205.07	1	<2.2E-16
	RLMlag	6.15	1	0.013
Anisotropy	LMerr	37704.35	1	<2.2E-16
	LMlag	37702.72	1	<2.2E-16
	RLMerr	40.77	1	0.000
	RLMlag	39.14	1	0.000
Alpha	LMerr	30245.40	1	<2.2E-16
	LMlag	26114.36	1	<2.2E-16
	RLMerr	4131.80	1	<2.2E-16
	RLMlag	0.76	1	0.382

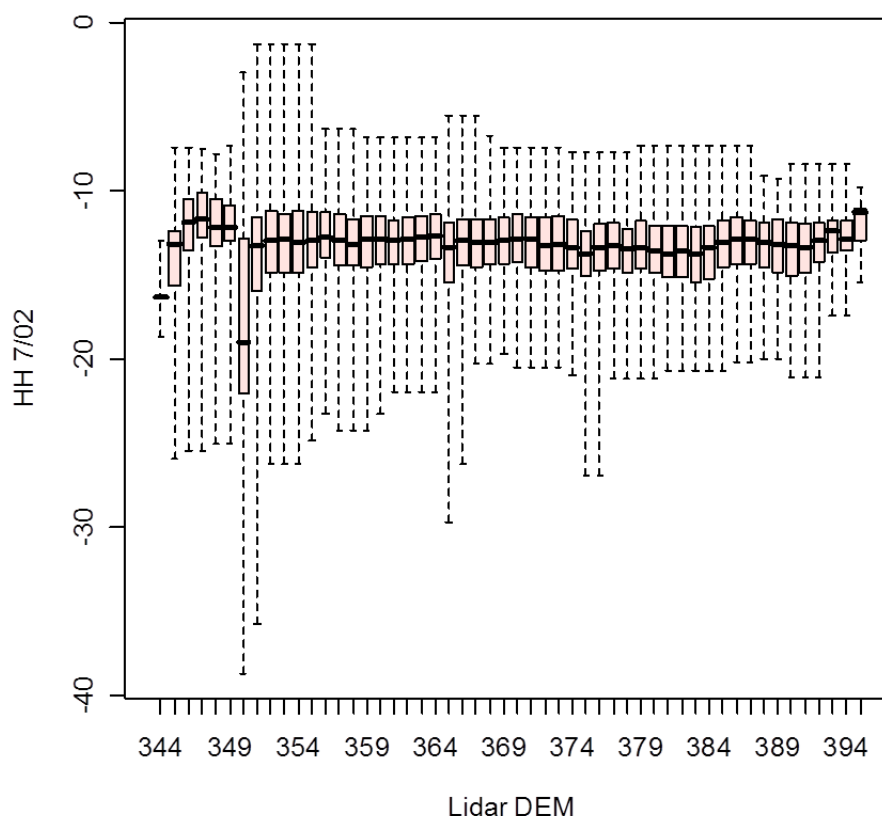
**Table 4.** Spatial Error Model (SEM) regression analysis for representative observations.

Dependent Variable	Independent Variable	Coefficient	Standard Error	Test Statistic	p-value	SEM AIC	OLS AIC
HH	(Intercept)	6.84	17.06	0.40	0.69	21,453.00	25,322.00
	B1	-0.10	0.01	-9.74	<2e-16	--	--
	Lambda	1.00	--	3870.40	<2e-16	--	--
HV	(Intercept)	-66.31	33.93	-1.95	0.05	16,956.00	23,356.00
	B1	-0.06	0.01	-9.17	<2e-16	--	--
	Lambda	1.00	--	6402.40	<2e-16	--	--
Entropy	(Intercept)	0.02	0.21	0.08	0.94	-13,616.00	-10,805.00
	B1	0.00	0.00	-0.94	0.35	--	--
	Lambda	1.00	--	2812.30	<2e-16	--	--
Anisotropy	(Intercept)	0.07	0.23	0.30	0.77	-13,949.00	-10,930.00
	B1	0.00	0.00	-1.77	0.08	--	--
	Lambda	1.00	--	3021.10	<2e-16	--	--
Alpha	(Intercept)	0.80	0.51	1.56	0.12	-4,433.90	-1,846.60
	B1	0.00	0.00	-2.42	0.02	--	--
	Lambda	0.99	--	2,589.40	<2e-16	--	--

The directional variograms of the sub-meter LiDAR at the mire show greater sensitivity to the features the LiDAR is observing (*i.e.*, “elevation”) relative to the PALSAR observations of scattering mechanisms of the mire according to the directional variograms (Figure 4). Most notably was the 135° directional variogram that distinctly captured relatively strong anisotropic behavior highlighting

surface hydrology patterns, or surface flow direction, that were notably in this direction as compared to other directions. The variogram assessment in this application shows that the LiDAR derived-elevation, which is also indicative of hydrogeomorphology, was slightly more sensitive to topographic structure compared to multitemporal filtered, fine-beam PALSAR sensitivity to mire scattering mechanisms at the given observation scales. Conversely, this implies that elevation is not the sole driver of vegetative structure.

**Figure 5.** Representative pattern of HH PALSAR backscatter response by elevation as measured by LiDAR. This pattern is similar across observation modes and DOY. As elevation increases the range of Palsar backscatter decreases into a finer distribution indicating the trend of structural attributes of the mire vegetative communities tends to become more homogeneous with less variability. Note the elevation (~350 m) of many water bodies causing a diverse PALSAR response.



Across observation modes and DOY the range of HH and HV decreases as elevation increases (Figure 5). This is not a result of topographic features influencing radiometry as the highest elevations of the actual mire and permafrost are gradual shifts and do not contain rock features. This corresponds with mire vegetation configuration, which is, in part, driven by a combination of elevation and hydrological fluctuations. At elevations near the 350 m zone the water table tends to create ponding which promotes herbaceous-emergent and erectly oriented edge species compositions (*Carex rotundata*, *Eriophorum vaginatum*, *Politrichum jensenii*). The dynamic hydrology (*i.e.*, water table depth, soil moisture, freeze/thaw) also promotes palsa and embankment collapse creating more complex scattering targets along with ecotonal species. However, the hydrogeomorphology, permafrost, and active later depth of the mire also create small ponding features at higher elevations.

Therefore, only using the LiDAR data individually to map surface hydrology would be inadequate for a thorough characterization of mire hydrology and dynamics due to the single overpass time of LiDAR, sensitivity of PALSAR to vegetative structure, and fact that elevation is not the sole driver of community composition.

Slightly higher than 350 m and adjacent to many ponding features, dry ombrotrophic, ombrominerotrophic, and ombrotrophic (*Empetrum hermaphroditum*, *Betula nana*, *Rubus chamaemorus*, *Eriophorum vaginatum*, *Carex rotundata*, *S. balticum*, *Drepanucladus schulzei*, and *Politrichum jensenii*) species dominate the hummock, wet, and semiwet peat soils [22] with the palsa patches underlain by permafrost. As the surface elevation increases at the mire, backscatter variability tends to become more uniform with backscatter minimum increasing, backscatter maximum and range decreasing, and the 25th and 75th percentile distribution becomes less variable (Figure 5). This supports the notion that geomorphic setting, measured in part by the LiDAR, is one key driver of surface water pooling and drainage, and thus, vegetative composition and configuration, which was captured by the PALSAR. At the same time this shows the use of both LiDAR and PALSAR are uniquely advantageous for interpretations of mire characteristics and ecology.

The PLR observation was early in the thawing stage (DOY 151) and therefore was not at a peak time for mapping maximum soil moisture across the mire. A sharp rise in soil moisture occurs near DOY 183; however, minimum daily temperature typically remains above freezing after DOY 145 and corresponds to divergence in net ecosystem production and gross primary production. Therefore, DOY 151 is suitable for mapping mire surface hydrology however precautions must be used in interpretations. The relatively low pedestal height (0.25) of the copolarized and (0.15) cross-polarized PLR signature shows the maximum return at the horizontal polarization was indicative of less complex single bounce scattering. This was due, in part, to an early thaw image as the double bounce of densely vegetated wetlands was not dominant and was uniform at elevations higher than most of the ponding areas (e.g., ~350 m a.s.l.). With increasing elevation, tall, erectly-oriented graminoids shift toward scrub-shrub communities at even higher elevations with occasional patches of barren rock. Canopy scattering was more apparent at higher elevations as visible in the green-yellow tones of Figure 6 compared to the blue-purple tones at lower elevations with surface scattering from water and the mesic and palsa regions underlain by permafrost.

The CP scattering decomposition histogram (Figure 7) indicates mostly surface scattering and medium entropy tend to dominate while vegetative scattering was present at smaller quantities. By using the LiDAR the vegetative scattering tended to occur at high elevations for DOY 151. This supports the interpretation that the dominant Bragg scatterer was the primary signal from peat moisture conditions and water table levels, much of which is over a subsurface permafrost layer especially when considering phenology (*i.e.*, freeze/thaw) at this DOY (151). Several ponds, with a distinct single bounce surface scattering response, are located at the site and this was evident in the PLR decomposition products by the dark purple-black colored patches dispersed across the image. The low alpha implies the mire site, as observed on DOY 151 by PALSAR, was largely a single-bounce scattering target lending itself to sensitivity to permafrost peat condition this time of year. These patterns are visually apparent in Figure 6 where the purple colors are present which also happens to be the location of a permafrost zone.

**Figure 6.** (a) PALSAR polarimetric (DOY: 151) Pauli Decomposition (Red: even bounce, Green: volume, Blue: surface bounce) highlighting scattering across the mire including permafrost areas. (b) High-resolution LiDAR characterized the mire surface and observed the majority of larger water bodies to reside near the 350 m elevation zone.

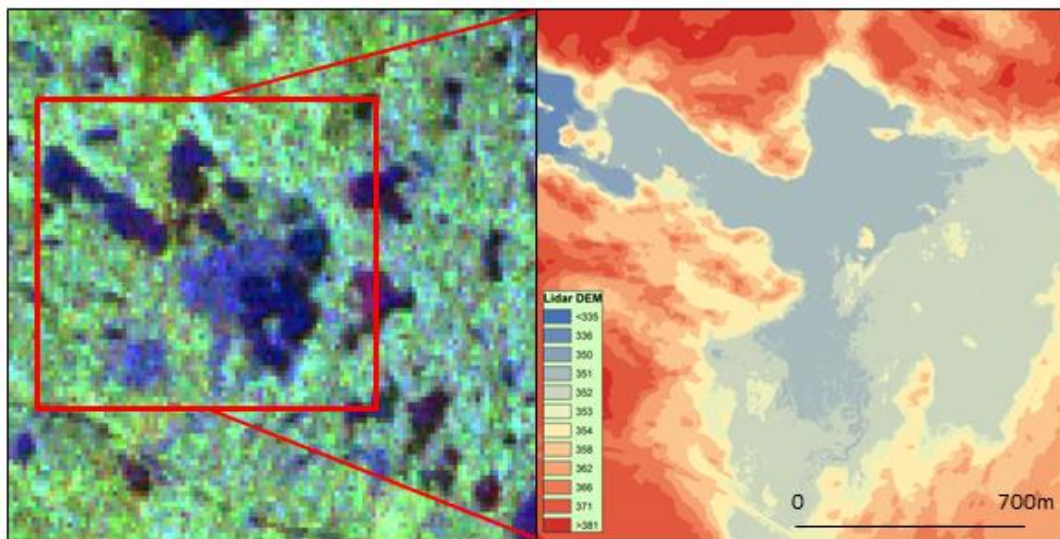
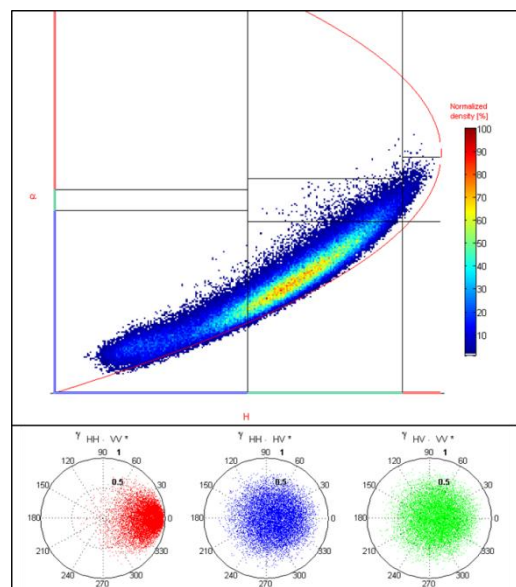


**Figure 7.** CP alpha ( $\alpha$ ) vs. entropy (H) density histogram and channel coherence illustrate scattering mechanisms at the mire. Surface scattering and primarily medium-to-low entropy tend to dominant while vegetative scattering was present. Image observation DOY 151 is relatively early in the thawing process for this particular site influencing scattering.



The CART classifications had overall accuracies between 70 to 86% and kappa between 64 to 80% using out-of-sample validation ( $n = 800$ ) with significant  $p$ -values ( $<0.00001$ ) (Table 5). The water class tended to have the highest class-level accuracies (sensitivity: 0.94, specificity: 0.97, positive prediction value: 0.92, negative prediction value: 0.98) which was not unexpected considering the unique scattering mechanisms of the water class compared to the other classes. An advantage of this

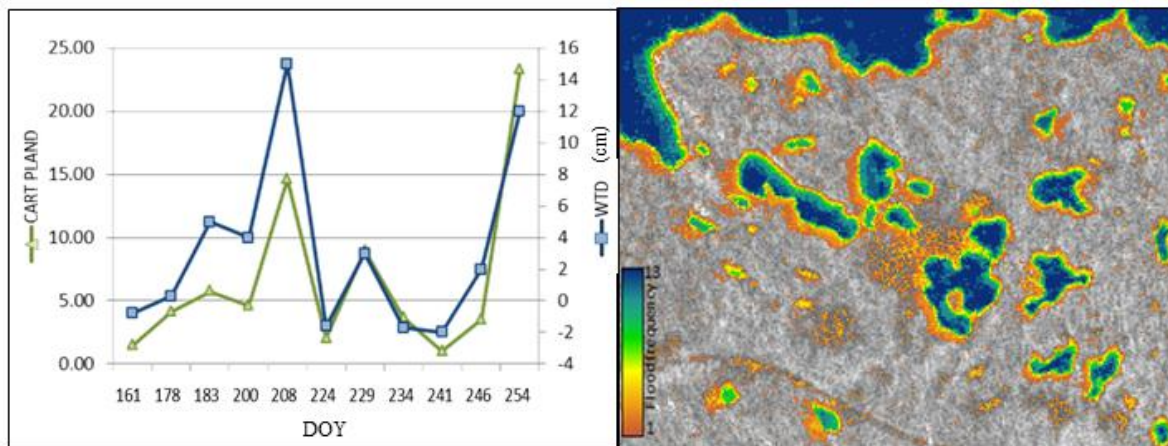
CART approach was that pixels receive a series of votes. This created not only a thematic map that was determined by the class with the maximum number of votes, but also a continuous likelihood map for each class that corresponds to the total number of votes. For mixed pixels, pixels with high soil moisture, or pixels with the presence of surface water the number of votes for the water class varied depending on how that pixel matched the training data (PALSAR and LiDAR products that vary by DOY).

**Table 5.** Representative CART error matrices.

Error Matrix for DOY 200					Error Matrix for DOY 161				
	1	2	3	4		1	2	3	4
1	184	25	2	0	1	187	13	0	0
2	12	139	0	60	2	13	116	0	28
3	4	0	198	0	3	0	0	200	0
4	0	36	0	140	4	0	71	0	172
Accuracy 0.8262 95% CI (0.7982, 0.8519) p-value < 2.2e-16 Kappa 0.7683					Accuracy 0.8438 95% CI (0.8167, 0.8682) p-value < 2.2e-16 Kappa 0.7917				
1	hummock/mosses and palsa (dry ombrotrophic)								
2	mesic (ombro-minerotrophic)								
3	open water								
4	graminoid (wet minerotrophic)								

The CART water maps were cross-referenced with field WTD observations from a wet site for all available corresponding time periods. While the number of samples limits the utilization of traditional goodness-of-fit measures, the WTD and fused LiDAR-PALSAR water maps match extremely well (Figure 8:  $R^2 = 0.86$ ,  $n = 11$ ); PLAND (“Percent of Landscape”) is an index common in landscape ecology that in this case is simply derived by averaging (pixels) the CART water class map across the mire study area. Each data point direction ( $\pm$ ) and magnitude of change to the next data point was found very consistent between the two datasets. Further, a small temporal window (May–September for 2008 and 2009) of available soil moisture data measured at palsa and sphagnum sites were strongly correlated ( $R^2$  0.69–0.78) with the WTD measurements. Therefore, the CART water maps were qualitatively strong and accurate indicators of soil moisture. Thus, in the dry ombrotrophic, ombro-minerotrophic, and ombrotrophic ecotonal communities including palsa bog underlain by permafrost, L-band had abilities to penetrate the vegetative canopy and characterize peat moisture levels that are driven largely by water table depth and precipitation. This supports similar findings that ALOS L-band has abilities to characterize inundation dynamics in high latitude wetlands [14,15].

**Figure 8.** The CART flood likelihood map Percent of Landscape (PLAND) metric had strong correspondence to Water Table Depth (WTD) measurements at the mire across the aggregated DOY (different years) calendar for corresponding periods. The flood frequency map indicates the percent a pixel was observed as flooded and as an indicator of soil moisture. Ponds, embankments, depressions, and several areas including surfaces over permafrost have noteworthy hydrological dynamics.



The applied results show that annual and interannual variability can vary by an order of magnitude and a hydrological surplus or deficit can occur early or late in the warm season. Figure 8 displays the flood likelihood values across the mire. Areas over a permafrost zone adjacent to water pools, that appears dark blue in Figure 6, were observed to have low to moderate fluctuating (appears green-yellow in Figure 6) hydroperiod conditions. Excluding surface water pools, this permafrost region of the mire tended to have a relatively dynamic hydroperiod during the aggregated warm season. The ability to remotely monitor peat hydroperiod over space and time successfully is important as our recent efforts to understand peatland C balance have shown that Net Ecosystem Exchange for the palsa areas were significantly lower (*i.e.*, greater uptake) in wetter years (*i.e.*, 2008) compared to drier years (*i.e.*, 2009) during key warm months [24]. The CART maps can also potentially provide an indicator of the active layer and permafrost degradation as wetness and the depth of the permafrost layer have been linked at this site [40]. These results have significant implications for the hydrological variability of high latitude wetlands and monitoring hydroperiod. This hydrological variability influences the partitioning of the soil into anoxic and oxic zones, and thus net greenhouse gas emissions, with a potential feedback to climate. It also influences rates of permafrost degradation, and thus soil wetness, again with potential feedbacks to the climate system.

In this application the information derived from both Lidar and PALSAR is enhanced when combined to more comprehensively characterize hydroperiod and related hydrogeomorphic conditions of the mire. The Lidar was primarily utilized to map topographic features, including surface flow paths, while PALSAR was primarily utilized to map surface and vegetative conditions, including hydroperiod, over time across the site. Together the sensors were able to extract useful and unique information that when combined enable a more thorough assessment of hydroperiod and hydrogeomorphic conditions. Neither sensor was capable of comprehensively mapping multiple hydrogeomorphic attributes (*i.e.*, topography and hydroperiod) at the mire; however, together a more

detailed characterization was feasible. For example, the single date Lidar was not capable of mapping hydrological attributes over time, while the fine-beam PALSAR was not capable of resolving topographic features influencing flow paths on the order of magnitude of sub-meter scale. In this application each sensor has strengths and limitations that were enhanced by the other sensor.

The approach described in this research application provides a useful spatiotemporal assessment of hydrological variability and hydrogeomorphic attributes of the mire. Ecologically, the results show that both datasets (*i.e.*, LiDAR and PALSAR) provide unique and valuable information for characterizing mire spatial structure and hydroperiod. These types of spatial databases will be useful for driving biogeochemical models and extrapolating field measurements. A qualitative comparison of the CART technique was performed against simple thresholding techniques that have been successful for mapping hydroperiod in agricultural systems. The thresholding values were based on the box and whisker plots (Figure 3) generated for each DOY observation. The CART substantially outperformed the thresholding technique as the WTD values did not correspond well with thresholding products of water for this site likely due to the thresholding values being generated from the open water class and not optimized to mesic or wet minerotrophic conditions with higher soil moisture.

#### 4. Conclusion

The high temporal frequency PALSAR and high spatial resolution LiDAR were integrated to successfully characterize the hydrogeomorphic conditions and hydrological variability of the high latitude mire in Sweden. Each sensor was shown to have individual strengths that were amplified when fused with the other sensor. The CART was particularly useful for ingesting different data modes and scales to seamlessly generate metrics sensitive to key wetland hydroperiod attributes. The L-band data was found to be quantitatively sensitive to water table depth and qualitatively sensitive to soil moisture as measured at the mire. These results support similar findings that have found L-band capable of penetrating peat and charactering moisture regimes. The maps generated in this application were useful for extrapolating valuable wetland ecosystem functions (e.g., hydroperiod) over space. Regions underlain by permafrost were shown to have noteworthy hydrological variability, which influences carbon storage, methane dynamics, and land-atmosphere feedbacks. Future efforts are focused on using the results of this research application for assessing impacts of climate change on carbon dynamics with process-based modeling tools and carrying out analysis at additional high latitude sites.

#### Acknowledgments

Support for this project was provided in part by the NASA Terrestrial Ecology program (NNX09AQ36G). ALOS PALSAR data were provided by JAXA EORC and the Kyoto & Carbon Initiative. The funding of the LIDAR survey and DEMs created from it, came from a number of agencies through a partnership of researchers. We acknowledge the contributions of the US Dept. of Energy, Office of Science (grant #ER64991) support to Changsheng Li and Steve Frolking, the Natural Sciences and Engineering Research Council of Canada, Discovery Grant to Nigel Roulet (McGill University); the Abisko Research Station supported at the time by the Royal Swedish Academy of Sciences, KVA; Patrick Crill (Stockholm University) by the Swedish Research Council, VR; Torben R. Christensen (Lund University) by the Swedish Research Council, VR; Håkan Olsson (Swedish

University of Agricultural Sciences) by the Swedish Environmental Protection Agency; and Andreas Persson's and Petter Pilesjö's research grants at the Lund University GIS Centre. Thanks to field staff Niklas Rakos, Hedvig Oste, and Oskad Bergkvist. Thanks to open source SAR software providers including Ridha Touzi for access to Polarimetric WorkStation, Alaska Satellite Facility for MapReady, and European Space Agency for PolSARpro. Thanks to two reviewers for providing thoughtful comments which improved the manuscript.

## References

1. Tarnocai, C.; Canadell, J.; Schuur, E.; Kuhry, P.; Mazhitova, G.; Zimov, S. Soil organic carbon pools in the northern circumpolar permafrost region. *Glob. Biogeochem. Cy.* **2009**, *23*, GB2023.
2. Grosse, G.; Harden, J.W.; Turetsky, M.R.; McGuire, A.D.; Camill, P.; Tarnocai, C.; Frohling, S.; Schuur, E.A.G.; Jorgenson, T. Vulnerability of high latitude soil organic carbon in North America to disturbance. *J. Geophys. Res.-Biogeosciences* **2011**, *116*, doi:10.1029/2010JG001507.
3. Zimov, S.; Schuur, E.; Chapin, F. Climate change: Permafrost and the global carbon budget. *Science* **2006**, *312*, 1612–1613.
4. Zhang, Q.; Melack, J.; Zimov, S.; Sakha, C.; Walter, K.; Butenhoof, C.; Khalil, A. Global methane emissions from wetlands, rice paddies, and lakes. *EOS Trans. AGU* **2009**, *90*, 37–38.
5. Frohling, S.; Talbot, J.; Jones, M.; Treat, C.; Kauffman, J.; Tuittila, E.; Roulet, N. Peatlands in the Earth's 21st century climate system. *Environ. Rev.* **2011**, *19*, 371–396.
6. Christensen, T.R.; Ekberg, A.; Ström, L.; Mastepanov, M.; Panikov, N.; Öquist, M.; Svensson, B.H.; Nykänen, H.; Martikainen, P.J.; Oskarsson, H. Factors controlling large scale variations in methane emissions from wetlands. *Geophys. Res. Lett.* **2003**, *30*, doi:10.1029/2002GL016848.
7. Whalen, S. Biogeochemistry of methane exchange between natural wetlands and the atmosphere. *Environ. Eng. Sci.* **2008**, *22*, 73–94.
8. Bourgeau-Chavez, L.; Smith, K.; Brunzell, S.; Richardson, C.; Romanowicz, E.; Kasischke, E. Remote monitoring of regional scale inundation patterns and hydroperiod in the Greater Everglades using synthetic aperture radar. *Wetlands* **2005**, *25*, 176–191.
9. Chapman, B.; Siqueira, P.; Freeman, A. The JERS Amazon Multi-Season Mapping Study (JAMMS): Observation strategies and data characteristics. *Int. J. Remote Sens.* **2002**, *23*, 1427–1446.
10. Kasischke, E.; Bourgeau-Chavez, L.; Rober, A.; Wyatt, K.; Wadington, J.; Turetsky, M. Effects of soil moisture and water depth on ERS SAR backscatter measurements from an Alaskan wetland complex. *Remote Sens. Environ.* **2009**, *113*, 1868–1873.
11. Novo, E.; Costa, M.; Mantovani, E.; Lima, I. Relationship between macrophyte stand variables and radar backscatter at L and C band, Tucuruí reservoir, Brazil. *Int. J. Remote Sens.* **2002**, *23*, 1241–1260.
12. Rosenqvist, A.; Finlayson, C.; Lowry, J.; Taylor, D. The potential of long-wavelength satellite-borne radar to support implementation of the Ramsar Wetlands Convention. *Aquat. Conserv.* **2007**, *17*, 229–244.
13. Whitcomb, J.; Moghaddam, M.; McDonlad, K.; Kellendorf, J.; Podest, E. Mapping vegetated wetlands of Alaska using L-band radar satellite imagery. *Can. J. Remote Sens.* **2009**, *35*, 54–72.

14. Touzi, R.; Deschamps, A.; Rother, G. Phase of target scattering for wetland characterization using polarimetric C-band SAR. *IEEE Trans. Geosci. Remote Sens.* **2009**, *47*, 3241–3261.
15. Touzi, R.; Gosselin, G.; Brook, R. Peatland Subsurface Water Flow Monitoring Using Polarimetric L-Band Palsar. In *Proceedings of 'PolInSAR 5th Int. Workshop on Science and Applications of SAR Polarimetry and Polarimetric Interferometry'*, Frascati, Italy, 24–28 January 2011.
16. Knight, J.; Dale, P.; Spencer, J.; Griffin, L. Exploring LiDAR data for mapping the micro-topography and tidal hydro-dynamics of mangrove systems: An example from southeast Queensland, Australia. *Estuar. Coast. Shelf Sci.* **2009**, *85*, 593–600.
17. Hasan, A.; Pilesjö, P.; Persson, A. The use of LIDAR as a data source for digital elevation models—A study of the relationship between the accuracy of digital elevation models and topographical attributes in northern peatlands. *Hydrol. Earth Syst. Sci. Discuss.* **2012**, *8*, 5497–5522.
18. Torbick, N.; Salas, W.; Hagen, S.; Xiao, X. Monitoring rice agriculture in the Sacramento Valley, USA with multitemporal PALSAR and MODIS imagery. *IEEE J. Sel. Top. Appl. Earth Obs. Remote Sens.* **2011**, doi:10.1109/JSTARS.2010.2091493.
19. Torbick, N.; Salas, W.; Xiao, X.; Ingraham, P.; Fearon, M.; Biradar, C.; Zhao, D.; Liu, Y.; Li, P.; Zhao, Y. Integrating SAR and optical imagery for regional mapping of paddy rice attributes in the Poyang Lake Watershed, China. *Can. J. Remote Sens.* **2011**, *37*, 17–26.
20. Bourgeau-Chavez, L.; Riordan, K.; Powell, R.; Miller, N.; Nowels, M. Improving Wetland Characterization with Multi-Sensor, Multi-Temporal SAR and Optical/Infrared Data Fusion. In *Advances in Geosciences and Remote Sensing*; inTech: Rijeka, Croatia, 2009; pp. 679–709.
21. Zwenzner, H.; Voigt, S. Improved estimation of flood parameters by combining space based SAR data with very high resolution digital elevation data. *Hydrol. Earth Syst. Sci.* **2009**, *13*, 567–576.
22. Johansson, T.; Malmer, N.; Crill, P.; Frisborgs, T.; Akerman, J.; Mastepanov, M.; Christensen, T. Decadal vegetation changes in a northern peatland, greenhouse gas fluxes and net radiative forcing. *Glob. Change Biol.* **2006**, *12*, 2352–2369.
23. Xiao, X.; Dorovskoy, P.; Biradar, C.; Bridge, E. A library of georeferenced photos from the field. *EOS Trans. AGU* **2011**, *92*, 453–454.
24. Olefeldt, D.; Roulet, N.; Bergeron, O.; Crill, P.; Bäckstrand, K.; Christensen, T. Net carbon accumulation of a high-latitude permafrost palsamire similar to permafrost-free peatlands. *Geophys. Res. Lett.* **2012**, *39*, L03501.
25. Bäckstrand, K.; Crill, P.; Jackowicz-Korczyński, M.; Mastepanov, M.; Christensen, T.; Bastviken, D. Annual carbon gas budget for a subarctic peatland, Northern Sweden. *Biogeosciences* **2010**, *7*, 95–108.
26. De Grandi, G.; Lee, J.; Schuler, D.; Nezry, E. Texture and speckle statistics in Polarimetric SAR synthesized images. *IEEE Trans. Geosci. Remote Sens.* **2003**, *41*, 2070–2088.
27. De Grandi, G.; Leysen, M.; Lee, J.; Schuler, D. Radar Reflectivity Estimation Using Multiplicative SAR Scenes of the Same Target: Technique and Applications. In *Proceedings of IEEE 1997 International Geoscience and Remote Sensing Symposium*, Singapore, 3–8 August 1997; pp. 1047–1050.
28. Brisco, B.; Kapfer, M.; Hirose, T.; Tedford, B.; Liu, J. Evaluation of C-band polarization diversity and polarimetry for wetland mapping. *Can. J. Remote Sens.* **2011**, *37*, 82–92.

29. Touzi, R.; Deschamps, A.; Rother, G. Wetland characterization using polarimetric Radasat-2 capability. *Can. J. Remote Sens.* **2007**, *33*, 56–67.
30. Cloude, S.R.; Pottier, E. A review of target decomposition theorems in radar polarimetry. *IEEE Trans. Geosci. Remote Sens.* **1996**, *34*, 498–518.
31. Touzi, R. Target scattering decomposition in terms of roll-invariant target parameters. *IEEE Trans. Geosci. Remote Sens.* **2007**, *45*, 73–84.
32. Meyer, F.; Nicoll, J. Prediction, detection, and correction of Faraday rotation in full-polarimetric L-band SAR data. *IEEE Trans. Geosci. Remote Sens.* **2008**, *46*, 3076–3086.
33. Torbick, N.; Becker, B.; Hession, S.; Qi, J.; Roloff, G.; Stevenson, J. Assessing invasive plant infestation and disturbance gradients in a freshwater wetland using a GIScience approach. *Wetl. Ecol. Manag.* **2010**, doi: 10.1007/s11273-009-9171-5.
34. Anselin, L. Spatial Statistical Modeling in a GIS Environment. In *GIS, Spatial Analysis and Modeling*; Maguire, D., Goodchild, M., Batty, M., Eds.; ESRI Press: Redlands, CA, USA, 2006; pp. 93–111.
35. Anselin, L.; Bera, A. Spatial Dependence in Linear Regression Models with an Introduction to Spatial Econometrics. In *Handbook of Applied Economic Statistics*; Ullah, A., Giles, D., Eds.; Marcel Dekker: New York, NY, USA, 1998; pp. 237–289.
36. Breiman, L. Random Forest. *Machine Learning* **2001**, *45*, 5–32.
37. Lawrence, R.; Wood, S.; Sheley, R. Mapping invasive plants using hyperspectral imagery and Breiman Cutler classifications (RandomForest). *Remote Sens. Environ.* **2006**, *100*, 356–362.
38. Watts, J.; Lawrence, R.; Miller, P.; Montagne, C. Monitoring of cropland practices for carbon sequestration purposes in north central Montana by Landsat remote sensing. *Remote Sens. Environ.* **2009**, *113*, 1843–1852.
39. Whitcomb, J.; Moghaddam, M.; McDonald, K.; Kellndorfer, J.; Podest, E. Mapping wetlands of Alaska from L-band SAR imagery. *Can. J. Remote Sens.* **2009**, *35*, 54–72.
40. Malmer, N.; Johansson, T.; Olsrud, M.; Christensen, T. Vegetation, climatic changes and net carbon sequestration in a north-Scandinavian subarctic mire over 30 years. *Glob. Change Biol.* **2005**, *11*, 1895–1909.